9 DMRG for Multiband Impurity Solvers

Hans Gerd Evertz

Institute for Theoretical and Computational Physics

Graz University of Technology, Austria

Contents

1   Introduction

The computationally most difficult task in Dynamical Mean Field Theory (DMFT) [1–4] is the calculation of the self energy $\Sigma(\omega)$ or, equivalently, the spectral function $A(\omega)$. For typical physically relevant systems with three or five orbital impurities, this becomes demanding, and the energy resolution of standard techniques has been limited. In this chapter, a new method is described, dubbed *Fork Tensor Product States* (FTPS) [5, 6], which is as efficient as the best established methods for multiple orbitals, but has much better energy resolution at large energies, by way of using real-time evolution of an excited state. It is based on so-called Matrix Product State (MPS) techniques [7], which are related to the Density Matrix Renormalization Group (DMRG) [8].

The new method and the results described in this chapter are largely the work of my former student Daniel Bauernfeind, described in detail in his Ph.D. thesis [9]. I would like to thank him very much for a great collaboration.

1.1   Impurity solvers in DMFT

For the description of a material in DMFT, one first calculates the band structure by some variant of Density-Functional Theory (DFT) and projects the spectrum onto a few low lying effective orbitals, from which an effective Hamiltonian is constructed. Some aspects of this procedure will be discussed later in the results section. DMFT then treats the effective Hamiltonian locally, for example on a single site, which will be discussed here. The effect of all other sites is subsumed by the interaction with an effective bath, resulting in an effective Anderson Impurity Model (AIM) like
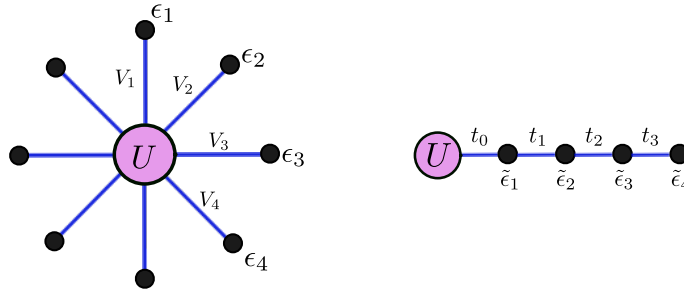
$$H_{\text{AIM}} = H_{\text{loc}} + \sum_k V_k \left(c_k^\dagger c_0 + h.c. \right) + \sum_k \varepsilon_k n_k \,. \tag{1}$$

Here, H_{loc} is the local interacting Hamiltonian, k is, e.g., a momentum space index numbering the noninteracting bath sites with local energy ε_k and occupation number $n_k = c_k^\dagger c_k$, and V_k is the hopping strength from the impurity (indicated by index zero) to the bath site.

For this model, the impurity spectral function $A(\omega)$ has to be calculated. It is then used together with the lattice structure of the material examined to determine new bath parameters V_k, ε_k in an iteration of the DMFT loop, until self-consistency is reached.

The bath represents a continuous spectrum of energies of the material around the impurity. Therefore the number N_B of sites in the bath and the corresponding spacing of the energies ε_k (as well as the choice of their values) limits the energy resolution which can be achieved. Often, the AIM is transformed into an equivalent representation as a *Wilson chain* [10, 11], i.e., a tight binding chain of length N_B with the impurity site coupled at one end.

Let us very briefly touch on some of the current impurity solvers and their strengths and weaknesses.

Fig. 1: *Anderson impurity model in two different representations. The circle marked by U represents the interacting site. Left:* star geometry, *a direct representation of Eq.* (1). *Right:* Wilson chain, *obtained after a unitary transformation.*

Continuous time quantum Monte Carlo

The state of the art work horse for DMFT calculations is probably Continuous Time Quantum Monte Carlo (CTQMC) [12, 13], usually in its CT-HYB variant. Here, the impurity problem is expressed in a Lagrangian formulation in continuous *imaginary time*, with a chain of length $\beta = 1/T$, the inverse of the temperature. The Green function $G(\tau)$ is measured, with statistical errors, in imaginary time, and needs to be transformed by a so-called analytic continuation to real time / real frequency, usually done with some variant of the Maximum Entropy method. This transformation is badly conditioned, especially for non-exact data. One of the consequences is that the energy resolution of the resulting spectrum becomes rather bad at large energies. We will see some examples in the section on results. The computational effort for CTQMC usually grows *exponentially* with the number of orbitals. An additional difficulty of CTQMC is a potential Monte-Carlo *sign problem* which then drastically limits the attainable inverse temperatures and numbers of orbitals.

Exact diagonalization / Configuration interaction

When there are not too many bath sites, the impurity spectral function $A(\omega)$ can be calculated with Exact Diagonalization (ED) [14–16], but will then consist of a limited number of delta-peaks. This can be improved, for example by using different bath discretizations within the same calculation or by optimizing the discretization in Configuration Interaction (CI) schemes [17, 18]. For a single orbital, spectra with good resolution have been achieved. However, for more orbitals, the energy resolution has been very limited by, for example, only 3 bath sites for 3 orbitals in Ref. [17].

Numerical Renormalization Group

The Numerical Renormalization Group (NRG) [10, 11] provides one of the standard approaches to impurity solvers. It works on the real frequency axis, successively integrating out degrees of freedom on high energy scales in a logarithmic fashion in a Wilson chain. It can provide very good energy resolution at low energies, even for several orbitals [19–21], but by construction is rather coarse at large energies. The number of orbitals enters exponentially into the computational effort. NRG amounts to a calculation with matrix product states (see below).

Dynamical DMRG

The so-called *Dynamical DMRG* (DDMRG) [22–25] and *Correction Vector* (CV) [26] approaches are variants of DMRG in which $A(\omega)$ can be calculated very precisely, although with some broadening, directly at a chosen frequency. However, a separate calculation is necessary for every frequency, so that multiple orbitals become infeasible.

Time evolution with matrix product states

Matrix product state methods also provide precise techniques to calculate the time evolution of pure states after a local excitation at the impurity site. Most methods have been developed in a closely related variant using Chebyshev polynomials [27–30] for up to 2 orbitals [30]. Direct real time evolution has been employed for one and two orbitals by Ganahl *et al.* [31], with very good energy resolution. However, the computational effort may grow exponentially with the number of orbitals and has in the past been far too large for more than two orbitals. More orbitals have only been reached in imaginary time [32], with associated energy resolution difficulties. In the present chapter we will see how to overcome these problems.

1.2   Calculation of impurity Green function in time evolution approaches

Impurity solvers using time evolution techniques employ the following general steps (leaving out spin and orbital indices for simplicity):

- Given the bath parameters, calculate the ground state $|\psi_0\rangle$ of the corresponding Anderson impurity model, with energy E_0.
- Apply an annihilation operator to obtain the excited state $|\psi_1\rangle = c_0|\psi_0\rangle$.
- Time evolve, i.e., calculate $e^{iHt}|\psi_1\rangle$.
- Calculate the overlap with $|\psi_1\rangle$, namely $G^<(t) = \langle\psi_1| e^{iHt} |\psi_1\rangle e^{-iE_0 t}$, which provides one part of the Green function.
- The resulting function $G(t)$ can, if desired, be post-processed with so-called *linear prediction* [27, 7, 31] (essentially a fit with $\mathcal{O}(100)$ Lorentzians) in order to further improve the energy resolution.
- Fourier transform to obtain $A(\omega)$.

More details can be found in Refs. [31, 5, 6, 9]. The Fork Tensor Product State (FTPS) approach to be described in the present chapter is based on the Matrix Product State (MPS) formalism, which we will therefore first discuss in some detail. For FTPS we will then introduce a special efficient tensor geometry. Both MPS (and DMRG) as well as FTPS require an essentially linear bath geometry. Yet we shall see that, quite surprisingly, it will be much more efficient to directly enumerate the sites k of the bath degrees of freedom (the so-called star geometry) along an artificial chain, instead of employing Wilson chains for the bath. At the end of the chapter we will discuss results and performance of the new method.

2 Matrix product state techniques

2.1 Matrix product states (MPS)

Matrix product states constitute the formalism behind DMRG. In order to understand the FTPS method, we need to go into some detail on the MPS approach. For a much more complete exposition, including all the references to the original literature, I refer to the great review by U. Schollwöck [7]. For a quick reading of this section, the graphical representation Fig. 2 and its explanation contain some of the most important aspects.

The state space of many-particle models grows exponentially with the number of particles involved. Such models can therefore be treated exactly only for very small systems. The MPS approach permits very precise and efficient approximations even for very large systems. It has allowed for, e.g., DMRG calculations of the ground state energy of Heisenberg models on several hundred sites to 10-digit precision, and can also be used to time-evolve a state. Note that a convenient library of tensor routines is available for such calculations [33].

2.1.1 Example: Heisenberg spin chain

In order to keep notation reasonably simple for the discussion of MPS, in this section we shall treat the one-dimensional spin-$1/2$ Heisenberg model with open boundary conditions

$$\hat{H} = \sum_{i=1}^{L-1} \hat{H}_i \quad \text{with} \quad \hat{H}_i = \frac{J_{xy}}{2} \left(S_i^+ S_{i+1}^- + S_i^- S_{i+1}^+ \right) + J_z S_i^z S_{i+1}^z , \tag{2}$$
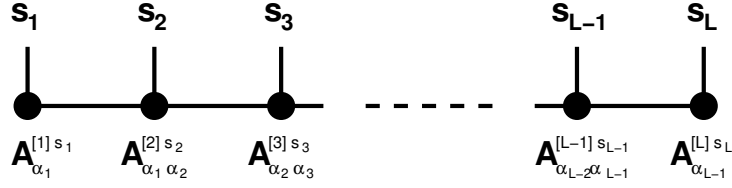
where $S_j^\pm = S_j^x \pm i S_j^y$, thus $S_j^+ |\downarrow\rangle_j = |\uparrow\rangle_j$ and $S_j^- |\uparrow\rangle_i = |\downarrow\rangle_j$. The representation of S_j^α in the z-basis at site j is $\sigma^\alpha/2$ (we leave out $\hbar$).

A chain of L sites has 2^L basis states, which are $|s_1, s_2, \ldots, s_L\rangle$ with $s_j \in \{\uparrow, \downarrow\}$ in the z-basis. In case of isotropic couplings $J_{xy} = J_z =: J$ we get $\hat{H} = J \sum_j \vec{S}_j \cdot \vec{S}_{j+1}$. This model is also a good approximation of the strongly repulsive Hubbard model ($U \gg t$) at half filling.

Note that on a one-dimensional chain, the Heisenberg model is equivalent to a model of tight-binding spinless fermions

$$\hat{H} = \sum_{j=1}^{L-1} t \left(c_j^\dagger c_{j+1} + h.c. \right) + V \hat{n}_j \hat{n}_{j+1} - \frac{V}{2} \left(\hat{n}_j + \hat{n}_{j+1} \right) + \frac{1}{4}$$

by the Jordan-Wigner transformation. With fermions, the only new aspect for MPS is the minus sign that appears upon interchanging two fermions. It can be dealt with by a suitable operator which we will discuss in the chapter on FTPS.

Fig. 2: *Graphical representation of an MPS. Black circles represent matrices A. Lines connected to the circles represent indices, which are summed over when the lines of two circles are connected. The horizontal set of circles and lines therefore represents the product of matrices in Eq. (4). The vertical lines denote the remaining physical indices s_i.*

2.1.2 Matrix product state ansatz

A general state of the Heisenberg chain is

$$|\psi\rangle = \sum_{s_1,s_2,\dots,s_L} c_{s_1,s_2,\dots,s_L} |s_1, s_2, \dots, s_L\rangle \tag{3}$$

with 2^L complex numbers as coefficients. We will now write the coefficients in a different way, as a product of matrices, with one matrix for every lattice-site. This can always be done exactly (see later) when the matrices are chosen big enough, namely up to $2^{L/2} \times 2^{L/2}$. We will later see that much smaller matrices ($\mathcal{O}(100) \times \mathcal{O}(100)$) can already provide an extremely good approximation to physically relevant states. The ansatz is

$$|\psi\rangle = \sum_{s_1,s_2,\dots,s_L} \sum_{\alpha_1,\alpha_2,\dots,\alpha_{L-1}} A^{[1]s_1}_{\alpha_1} A^{[2]s_2}_{\alpha_1,\alpha_2} A^{[3]s_3}_{\alpha_2,\alpha_3} \dots A^{[L-1]s_{L-1}}_{\alpha_{L-2},\alpha_{L-1}} A^{[L]s_L}_{\alpha_{L-1}} |s_1, s_2, \dots, s_L\rangle. \tag{4}$$

The A can be taken to be square matrices (except for the first and last A, which are vectors), and $\alpha_j = 1 \dots \chi$ are the matrix indices. The upper index $[j]$ numbers the lattice sites. The matrices A usually differ from site to site. At each site j, there are two matrices, $A^{[j]\uparrow}$, and $A^{[j]\downarrow}$, corresponding to the values $s_j = \uparrow$ and $s_j = \downarrow$ in the basis vector $|s_1, s_2, \dots, s_L\rangle$. For a given state, the matrices A are not unique: one can replace any pair of matrices $A^{[j]} A^{[j+1]}$ by $(A^{[j]} X) (X^{-1} A^{[j+1]})$, with any invertible matrix X. It is very helpful to denote this ansatz for the coefficients in a graphical way, as shown in Fig. 2. Let us look at some simple examples.

• *Single basis state (product state)* A state like $|\downarrow\downarrow\uparrow\downarrow\uparrow\downarrow\rangle$ is called "product state" since it can be written as a product $|\downarrow\rangle_1 |\downarrow\rangle_2 |\uparrow\rangle_3 |\downarrow\rangle_4 |\uparrow\rangle_5 |\downarrow\rangle_6$ and it does not contain any linear combination.

$|\psi\rangle$	=	|	$\downarrow$	$\downarrow$	$\uparrow$	$\downarrow$	$\uparrow$	$\downarrow$	$\rangle$
j	=		1	2	3	4	5	6	
$A_j^\uparrow$	=		0	0	1	0	1	0	
$A_j^\downarrow$	=		1	1	0	1	0	1	

The "matrices" A are just single numbers here.

- *Singlet, L=2 sites*

$$|\psi\rangle \;=\; \frac{1}{\sqrt{2}}\; \big(\; |\quad \uparrow\qquad \downarrow\qquad \rangle$$
$$-\;|\quad \downarrow\qquad \uparrow\qquad \rangle\;\big)$$

$$A_j^\uparrow \;=\; (1,0),\qquad -\binom{0}{1}\Big/\sqrt{2}$$

$$A_j^\downarrow \;=\; (0,1),\qquad \binom{1}{0}\Big/\sqrt{2}$$

- *Nonlocal singlet*

$$|\psi\rangle \;=\; \tfrac{1}{\sqrt{2}}\;\big(\; |\;\downarrow\;\downarrow\;\uparrow\qquad \downarrow\qquad \downarrow\qquad \downarrow\qquad \downarrow\;\downarrow\;\rangle$$
$$-\;|\;\downarrow\;\downarrow\;\downarrow\qquad \downarrow\qquad \downarrow\qquad \uparrow\qquad \downarrow\;\downarrow\;\rangle\;\big)$$

$$A_j^\uparrow \;=\; 0,\;\;0,\;\;(1,0),\;\;\begin{pmatrix}0&0\\0&0\end{pmatrix},\;\;\begin{pmatrix}0&0\\0&0\end{pmatrix},\;\;-\binom{0}{1}\Big/\sqrt{2},\;\;0,\;\;0$$

$$A_j^\downarrow \;=\; 1,\;\;1,\;\;(0,1),\;\;\begin{pmatrix}1&0\\0&1\end{pmatrix},\;\;\begin{pmatrix}1&0\\0&1\end{pmatrix},\;\;\binom{1}{0}\Big/\sqrt{2},\;\;1,\;\;1$$

2.1.3 Singular value decomposition (SVD)

The SVD is an extremely important and versatile tool from linear algebra and the central technical ingredient of MPS techniques. It is different from the familiar eigenvalue decomposition (see below), and it exists for every real or complex matrix. It is widely used for, e.g., image processing, signal processing, optimizations, etc. *Every* real or complex $n \times m$ matrix M can be decomposed like

$$M \;=\; U\,D\,V^\dagger \tag{5}$$

with a diagonal matrix D that contains only *positive real numbers* (or zero), which are called the *singular values* of M. It is of dimension $N = \min(n,m)$. Furthermore,

$$U^\dagger U = \mathbb{1},\;\; V^\dagger V = \mathbb{1},\;\; D = \begin{pmatrix} \lambda_1 & & & & & \\ & \ddots & & & & \\ & & \lambda_r & & & \\ & & & 0 & & \\ & & & & \ddots & \\ & & & & & 0 \end{pmatrix}. \tag{6}$$

We will always order $\lambda_1 \geq \lambda_2 \geq \cdots \geq \lambda_r > \lambda_{r+1} = 0 = \cdots = \lambda_N = 0.$. The number r of non-zero entries λ is called the rank of the matrix M, which need not be square. When, e.g.,

$m \leq n$, the SVD looks like $\boxed{\text{M}} = \boxed{\text{U}}\;\boxed{\text{D}}\;\boxed{V^\dagger}$ and $V^\dagger$ cannot be unitary. This version of the SVD, with (in general) non-square matrices U and $V^\dagger$, is called a "thin SVD". The values λ_i are uniquely determined. The matrices U and $V^\dagger$ are not unique: within each subspace (dimension ≥ 1) of equal singular values, one can multiply U with a unitary matrix and $V^\dagger$ with the inverse, without changing M. When M is real, then U and $V^\dagger$ can also be chosen real. When M is real and quadratic, then U and $V^\dagger$ are rotations (basis transformations), and D scales the directions in the intermediate basis. The eigenvalue decomposition of matrices $M^\dagger M$ and $M M^\dagger$ both have eigenvalues λ_j^2. When M is quadratic and all eigenvalues are ≥ 0, then the eigenvalue decomposition $M = UDU^\dagger$ is the same as the SVD.

The computational cost of a SVD is $\min(mn^2, m^2n)$. Many applications of the SVD involve **truncation**: one replaces small singular values by zero. This provides an *approximation* to M, which is usually very good and often of *far* smaller dimension, providing for much lower computational cost.

Representation of the SVD with square matrices

When M is not quadratic, then either U or $V^\dagger$ is not quadratic in the SVD $M = UDV^\dagger$. Alternatively, one can write the SVD with *unitary* quadratic matrices $\tilde{U}$ and $\tilde{V}$:

$$M = UDV^\dagger \;=\; \tilde{U}\tilde{D}\tilde{V}^\dagger \tag{7}$$

This can be interpreted as a basis transformation by $\tilde{V}^\dagger$, a weighting of directions by $\tilde{D}$, and another basis transformation by $\tilde{U}$. When M is $m \times n$ dimensional, then $\tilde{U}$ is $m \times m$, $\tilde{D}$ is $m \times n$, and $\tilde{V}^\dagger$ is $n \times n$.

- Case $m \leq n$: $\boxed{\text{M}} = \boxed{U}\;\boxed{\text{D}\!-\!000}\;\boxed{\begin{array}{c}V^\dagger \\ \hline (\text{rest})\end{array}}$

  In this case, $\tilde{U} = U$. The lower rows of $\tilde{V}^\dagger$ contain extra eigenvectors, beyond those in $V^\dagger$. They do not contribute to M because of the zeroes in $\tilde{D}$. Since the eigenvectors in $\tilde{V}^\dagger$ are orthogonal, the application of M to such a vector gives zero, i.e., they belong to the *null space* of M. (The directions j beyond the rank r, with vanishing singular value $\lambda_{j>r} = 0$ also belong to the null space). When considering the action of M on the full vector space, this null space can be ignored (see below).

- Case $m \geq n$: $\boxed{\text{M}} = \boxed{U \,\big|\, (\text{rest})}\;\boxed{\begin{array}{c}\text{D} \\ \hline 0\end{array}}\;\boxed{V^\dagger}$

  Now $\tilde{V} = V$.

Pseudoinverse

We first discuss the case of a square matrix M. Formally, the inverse is

$$M^{-1} = \left(\tilde{U} \, \tilde{D} \, \tilde{V}^\dagger \right)^{-1} = \tilde{V} \, \tilde{D}^{-1} \, \tilde{U}^\dagger, \tag{8}$$

since $\tilde{U}$ and $\tilde{V}$ are unitary. But the matrix M can contain singular values $\lambda_{j>r} = 0$. In these directions j, M does not act, and the inverse $\tilde{D}^{-1}$ would contain infinity.
It is much better to *exclude this null space* completely also from the inverse, i.e., to set $\tilde{D}^{-1}$ to zero there. This is called the *pseudoinverse*

$$\lambda_j \mapsto \frac{1}{\lambda_j}, \quad \text{but} \quad 0 \mapsto 0. \tag{9}$$

In practice, one maps singular values to zero when they are below some threshold (e.g. 10^{-10}). Using the pseudoinverse, $M^{-1}M$ becomes

$$M^{-1}M = \tilde{V} \, \tilde{D}^{-1} \, \tilde{U}^\dagger \, \tilde{U} \, \tilde{D} \, \tilde{V}^\dagger \; = \; \begin{pmatrix} 1 & & & & & \\ & \ddots & & & & \\ & & 1 & & & \\ & & & 0 & & \\ & & & & \ddots & \\ & & & & & 0 \end{pmatrix} \; = \; \dots \; = \; M \, M^{-1} \tag{10}$$

in which only (up to) the first r components correspond to the unity matrix, while the rest vanishes. The same considerations apply when M is not square, $n > m$ or $m > n$. Then $M^{-1}M$ is an $n \times n$ matrix. and MM^{-1} is $m \times m$. They are both of the form Eq. (10).

2.1.4 Schmidt decomposition, reduced density matrix, and entanglement

Consider any quantum-mechanical system and two arbitrarily chosen subsystems A and B, for instance the left and right side of a one dimensional chain with some arbitrary split. Let $|j\rangle_A$ be the orthonormal basis states of subsystem A, and $|k\rangle_B$ those of subsystem B. Then a general pure state of the total system is

$$|\Psi\rangle = \sum_{j,k} c_{jk} \, |j\rangle_A \, |k\rangle_B, \tag{11}$$

where c_{jk} are coefficients. We now regard c_{jk} as a matrix and look at its singular value decomposition

$$c_{jk} = \tilde{U} \, \tilde{D} \, \tilde{V}^\dagger, \quad \text{with } \tilde{U} \text{ and } \tilde{V} \text{ unitary.} \tag{12}$$

Written in matrix components, this becomes $c_{jk} = \sum_{\alpha=1}^{\chi} \lambda_\alpha \, \tilde{U}_{j\alpha} \, (\tilde{V}^\dagger)_{\alpha k}$, where χ is the rank of the matrix c_{jk}, the so called Schmidt-rank. Since $\tilde{U}$ and $\tilde{V}$ are unitary, it is possible to perform two basis transformations: $|A\rangle_\alpha := \sum_j \tilde{U}_{j\alpha}|j\rangle_A$ and $|B\rangle_\alpha := \sum_k (\tilde{V}^\dagger)_{\alpha k}|k\rangle_B$ and express the state $|\Psi\rangle$ in the new basis

$$|\Psi\rangle = \sum_{\alpha=1}^{\chi} \lambda_\alpha \, |A\rangle_\alpha \, |B\rangle_\alpha, \quad \text{with } \chi \leq \min(\dim(A), \dim(B)). \tag{13}$$

This Schmidt-decomposition of a general state $|\Psi\rangle$ always exists. The normalization $\langle \Psi \,|\, \Psi \rangle = 1$ implies

$$\sum_\alpha \lambda_\alpha^2 = 1 \,. \tag{14}$$

Reduced density matrix of a pure state

The density matrix of a *pure* state is $\hat{\rho} = |\Psi\rangle\langle\Psi|$, which can be written

$$\hat{\rho} = \sum_{\alpha=1}^{\chi} \sum_{\beta=1}^{\chi} \lambda_\alpha \lambda_\beta |A\rangle_\alpha |B\rangle_\alpha \,_\beta\langle A| \,_\beta\langle B| \,.$$

The *reduced density matrix* for the subsystem A is

$$\hat{\rho}_A = \text{tr}_B\, \hat{\rho} = \sum_\gamma \,_\gamma\langle B|\hat{\rho}|B\rangle_\gamma = \sum_{\gamma=1}^{\chi} \lambda_\gamma^2 \,|A\rangle_\gamma \,_\gamma\langle A| \,, \tag{15}$$

since the bases $|A\rangle$ and $|B\rangle$ are orthonormal. This is a sum over eigenvalues λ_γ^2 times a corresponding projection operator $|A\rangle_\gamma \,_\gamma\langle A|$. When the Schmidt rank χ is larger than one, the state is entangled and the reduced density matrix represents a mixed state, as we will see next.

Von Neumann entanglement entropy

Similar in definition to the entropy of a statistical system $S = -\,\text{tr}(\hat{\rho}\ln\hat{\rho})$, the von Neumann entanglement entropy between two subsystems A and B is defined as the entropy of the reduced density matrix:

$$S_A := -\,\text{tr}_A(\hat{\rho}_A \ln\hat{\rho}_A) \tag{16}$$

When the Schmidt decomposition of $|\psi\rangle$ and thus the reduced density matrix Eq. (15) is known, the von Neumann entropy is simply

$$S_A = -\sum_{\gamma=1}^{\chi} \lambda_\gamma^2 \ln\lambda_\gamma^2 = S_B \,. \tag{17}$$

S_A takes its maximum possible value of $\ln\chi$ when all λ_γ are of equal value. Note that the entanglement entropy between two subsystems is invariant under unitary transformations *within* a subsystem, but usually *not* under a transformation which mixes both subsystems, like e.g., a spatial Fourier transform.

Examples for a two site system

For a *product state,* $|\Psi\rangle = |\uparrow_A\uparrow_B\rangle = |\uparrow\rangle_A|\uparrow\rangle_B$ is already the Schmidt decomposition. The reduced density matrix is $\hat{\rho}_A = |\uparrow\rangle_A \,_A\langle\uparrow|$, which is a pure state, and the entanglement entropy between the two sites is $S_A = S_B = -1^2 \ln 1^2 = 0$.

For a *singlet,* $|\Psi\rangle = \frac{1}{\sqrt{2}}\big(|\uparrow\rangle_A|\downarrow,\rangle_B - |\uparrow\rangle_B|\downarrow\rangle_A\big)$ is also already the Schmidt decomposition, the reduced density matrix is $\hat{\rho}_A = \sum_{\alpha=1}^{2} \lambda_\alpha^2|A\rangle_\alpha \,_\alpha\langle A| = \frac{1}{2}\big(|\uparrow\rangle_A \,_A\langle\uparrow| + |\downarrow\rangle_A \,_A\langle\downarrow|\big)$, which in matrix notation is one half the unit matrix, and the entanglement entropy is $S_A = -2\,\frac{1}{2}\ln\frac{1}{2} = \ln 2$.

2.2   Different MPS representations of a state

2.2.1   Exact representation

The coefficients of any pure state $|\Psi\rangle = \sum_{s_1...s_L} c_{s_1...s_L} |s_1 \ldots s_L\rangle$ can be written as a "matrix product state" by going through the system site by site and performing Schmidt decompositions, i.e., basis transformations, at each site.

First site. We treat the coefficients $c_{s_1,(s_2...s_L)}$ as a matrix with row index s_1 and column index $(s_2 \ldots s_L)$ and apply an SVD

$$c_{s_1,(s_2...s_L)} \;=\; \sum_{\alpha_1=1}^{2} \underbrace{U^{[1]}_{s_1\alpha_1}}_{\text{2x2 matrix}} \lambda^{[1]}_{\alpha_1} V^{\dagger}_{\alpha_1(s_2...s_L)}$$

The upper index $[1]$ denotes the first lattice site. Since the index s_1 has only two values, $s_1 = \uparrow$ and $s_1 = \downarrow$, the matrix $U^{[1]}$ is (2×2) dimensional. We split it into two (1×2)-matrices $A^{[1]\uparrow}$ and $A^{[1]\downarrow}$ for the two spin components $\uparrow$ and $\downarrow$.

U is a unitary matrix. It contains a basis transformation from the basis $s_1 = \uparrow$, $s_1 = \downarrow$ to a new basis with indices $\alpha_1 = 1, 2$. Similarly, $V^{\dagger}$ defines a *basis transformation* on the vectors $|s_2, s_3, \ldots, s_L\rangle$, i.e., we get the Schmidt decomposition

$$|\Psi\rangle = \sum_{\alpha_1=1}^{2} \lambda^{[1]}_{\alpha_1} |\Phi^L_{\alpha_1}\rangle |\Phi^R_{\alpha_1}\rangle, \tag{18}$$

where $L(R)$ denote the left(right) subsystem.

Second site. We now regard $\lambda_{\alpha_1} V^{\dagger}_{\alpha_1(s_2...s_L)}$ (including the diagonal matrix λ) as a matrix element with row index $(\alpha_1 s_2)$ and column index $(s_3 \ldots s_L)$ and decompose it with an SVD

$$\lambda_{\alpha_1} V^{\dagger}_{\alpha_1(s_2...s_L)} \;=\; \sum_{\alpha_2=1}^{4} \underbrace{U^{[2]}_{(\alpha_1 s_2)\alpha_2}}_{\text{4x4 matrix}} \lambda^{[2]}_{\alpha_2} V^{\dagger}_{\alpha_2(s_3...s_L)}.$$

The summation index α_2 now goes up to 4, because of the possible combinations of $\alpha_1 = \{1, 2\}$ and $s_2 = \{\uparrow, \downarrow\}$.[1] The 4×4 matrix $U^{[2]}$ is again unitary and a basis transformation from $\{\alpha_1 s_2\}$ to $\{\alpha_2\}$ which we split up into two 2×4 matrices $A^{[2]\uparrow}$ and $A^{[2]\downarrow}$ for the two spin indices s_2

---

[1]The actual range of α can be smaller, when the coefficients of $|\Psi\rangle$ are such that the SVD has a lower rank, e.g., for a product state (rank 1).

After iteration up to site j. we get the following representation of the state $|\Psi\rangle$

$$|\Psi\rangle = \sum_{s_1...s_L} \sum_{\alpha_1} \overset{2}{\sum_{\alpha_2}} \overset{4}{\sum_{\alpha_3}} \overset{8}{\cdots} U^{[1]}_{s_1\alpha_1} U^{[2]}_{(\alpha_1 s_2)\alpha_2} \cdots U^{[j]}_{(\alpha_{j-1}s_j)\alpha_j} \lambda^{[j]}_{\alpha_j} V^\dagger_{\alpha_j(s_{j+1}...s_L)} |s_1 \ldots s_L\rangle. \quad (19)$$

This is also a Schmidt decomposition of $|\Psi\rangle$, between sites j and $j+1$. By splitting up each U-matrix into two distinct matrices for $\uparrow$ and $\downarrow$ spin indices, we can also write

$$U^{[1]}_{s_1\alpha_1} U^{[2]}_{(\alpha_1 s_2)\alpha_2} U^{[3]}_{(\alpha_2 s_3)\alpha_3} \cdots = A^{[1]s_1}_{\alpha_1} A^{[2]s_2}_{\alpha_1\alpha_2} A^{[3]s_3}_{\alpha_2\alpha_3} \cdots$$

Exact MPS representation of $|\Psi\rangle$. Continuing until the last lattice site, we find that indeed an arbitrary state $|\Psi\rangle$ can be represented exactly by a matrix product state

$$|\Psi\rangle = \sum_{s_1...s_L} \sum_{\{\alpha_i\}} A^{[1]s_1}_{\alpha_1} A^{[2]s_2}_{\alpha_1\alpha_2} A^{[3]s_3}_{\alpha_2\alpha_3} \cdots A^{[L-1]s_{L-1}}_{\alpha_{L-2}\alpha_{L-1}} A^{[L]s_L}_{\alpha_{L-1}} \; |s_1 \ldots s_L\rangle \quad (20)$$

represented graphically in Fig. 2. The range of the intermediate indices α_i is equal to the rank of the corresponding SVD. Note that between sites $L-1$ and L, this rank is a most 2, and between sites $L-2$ and $L-1$, it is at most 4. Thus, an *exponentially large maximum rank of up to* $2^{L/2}$ is reached in the middle of the chain for a general state.

2.2.2 Left-Normalization

Each of the matrices $U^{[i]}$ comes from an SVD and therefore satisfies $U^{[j]\dagger}U^{[j]} = \mathbb{1}$, which also provides for normalized basis transformations. In terms of the matrices $A^{[j]}$ this becomes

$$\sum_{s_j} A^{[j]s_j\dagger} A^{[j]s_j} = \mathbb{1} \quad (21)$$
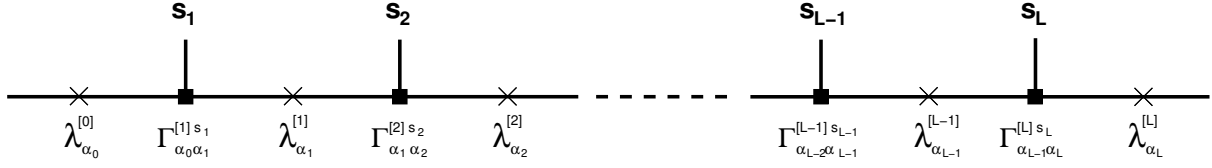
Written in matrix components, this equation reads

$$\sum_{s_j, a_{j-1}} A^{*[j]s_j}_{\alpha_{j-1}\alpha'} A^{[j]s_j}_{a_{j-1}\alpha} = \delta_{\alpha\alpha'} \quad \text{or graphically} \quad \alpha_{j-1} \;\; \left[\begin{array}{c} A^{[i]} \, \star \;\; \alpha'_j \\ s_j \\ A^{[i]} \;\; \alpha_j \end{array}\right] = \delta_{\alpha\alpha'}, \quad (22)$$

In the graphical representation, closed lines imply a summation. The normalization of the whole MPS, $\langle\Psi|\Psi\rangle = 1$, can now be deduced in a simple way, by applying the graphical form of Eq. (22) site by site. The state Eq. (4) and Fig. 2, written with A-matrices, is called *left-normalized*.

2.2.3 Canonical form of an MPS

Each Schmidt decomposition in the derivation of the MPS also gave us the singular values λ_α, i.e., information about the reduced density matrix at that step. We now write this information explicitly in the MPS. We take the singular values λ_α out of the A-matrices; this defines new matrices Γ

$$A^{[j]s_j}_{\alpha_{j-1}\alpha_j} =: \lambda^{[j-1]}_{\alpha_{j-1}} \Gamma^{[j]s_j}_{\alpha_{j-1}\alpha_j} \quad (23)$$

Fig. 3: *Graphical representation for the canonical form of MPS matrices.*

When the A-matrices are given, one can obtain the Γ matrices by multiplying A with the *pseudoinverse* of λ. Graphically, the "MPS state" (actually the coefficient $c_{s_1 s_2 \ldots s_L}$) is shown in Fig. 3, where we the diagonal denote λ-matrices by crosses, and Γ-matrices by squares. The $\lambda^{[j]}$ are located between sites j and $j+1$. They are the singular values of the Schmidt decomposition at that bond, $c_{s_1 s_2 \ldots s_L} = U \lambda V^\dagger$. In a product state, all $\Gamma^{[i]}$ are numbers 0 or 1, and all $\lambda^{[i]} = 1$. Since the first "matrix" $A^{[1] s_1}_{\alpha_1}$ is just a vector, the first index α_0 on $\Gamma^{[1] s_1}_{\alpha_0 \alpha_1}$ is superfluous. We still write $\Gamma^{[1] s_1}_{\alpha_0 \alpha_1}$ as a matrix, for easier notation later on, by letting the index α_0 only have one value $\alpha_0 = 1$ and $\lambda^{[0]}_{\alpha_0} \equiv 1$. Similarly, α_L has only the one value $\alpha_L \equiv 1$ and $\Gamma^{[1] s_1}_{\alpha_{L-1} \alpha_L}$ is actually a vector. At the right hand side we have introduced a final $\lambda^{[L]}_{\alpha_L} \equiv 1$. The normalization Eq. (22) now becomes an equation for Γ and λ, shown below on the left hand side

$$\sum_{s_j} \left(\Gamma^{[j] s_j}\right)^\dagger \left(\lambda^{[j-1]}\right)^2 \Gamma^{[j] s_j} = \mathbb{1} \qquad \sum_{s_j} \Gamma^{[j] s_j} \left(\lambda^{[j]}\right)^2 \left(\Gamma^{[j] s_j}\right)^\dagger = \mathbb{1} \qquad (24)$$

A similar normalization can also be shown to hold when summing over the second matrix index of $\Gamma^{[j]}$ by an iterative construction of the MPS from the right. This normalization is displayed on the right side of the equation above.

2.2.4 B-matrices, right-normalization, and mixed normalization

Instead of combining $A^{[j]} = \lambda^{[j-1]} \Gamma^{[j]}$ as in Eq. (23), one can group the matrices of the canonical representation via $B^{[j]} = \Gamma^{[j]} \lambda^{[j]}$, so that instead of Eq. (4) we get an equivalent product of B-matrices for the coefficients of $|\psi\rangle$. The B-matrices are *right-normalized*, as spelled out on the right side of Eq. (24).

In DMRG, the coefficients of states are usually expressed in the so-called *mixed-canonical* form $AA \ldots A \lambda B \ldots BB$ which follows directly from the canonical form in Fig. 3. The diagonal matrix λ contains the singular values of a Schmidt decomposition at the corresponding bond.

An unnormalized state can be brought into one of the canonical forms essentially by repeating an analogue of the steps outlined in section 2.2.1: successive SVDs from one end to the other.

Truncation

In order to achieve an efficient representation of a state, with relatively small matrices, we can approximate the state by discarding small singular values λ_α. This needs to be done in the canonical or mixed canonical representation, in which the λ_α do contain the Schmidt singular values. When all $\lambda_{\alpha>\alpha_0}^{[j]}$ are discarded, the matrices $\Gamma^{[j]}$ and $\Gamma^{[j+1]}$ can be *truncated* correspondingly beyond matrix index α_0. One can either discard values below a certain threshold ε (e.g. 10^{-10}), which results in a varying matrix dimension, or one can set a maximum matrix dimension $\chi_{\max}$ beyond which all singular values are discarded.

The quality of the approximation is related to how much of the reduced density matrix $\rho = \text{diag}(\lambda_1^2, \lambda_2^2, \dots)$ is discarded. This can be quantified by the so-called **truncated weight**

$$t_w = 1 - \sum_{\alpha=1}^{\chi_{\max}} \lambda_\alpha^2, \tag{25}$$

which should stay below some small threshold like $\ll 10^{-8}$ for precise calculations. In order to keep the state normalized, we have to re-normalize the remaining λ_α

$$\lambda_\alpha \ \to \ \lambda_\alpha/\sqrt{1-t_w}\,, \quad \text{so that} \quad \sum_\alpha \lambda_\alpha^2 = 1\,. \tag{26}$$

The normalizations of the A-matrices and the Γ-matrices are unaffected by the truncation, except that the matrix $\mathbb{1}$ in Eq. (21) is also truncated.

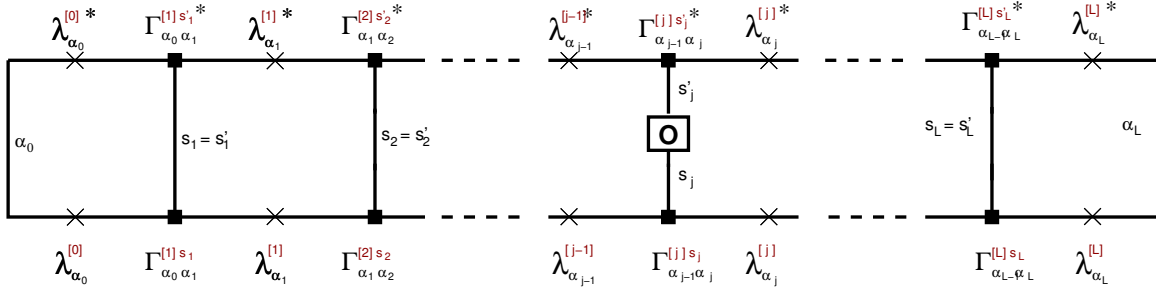**How large do the matrices need to be?**

The discarded weight t_w is small when the singular values λ_α decay quickly. This is the case when the entanglement entropy Eq. (17), $S_A = -\sum_{\gamma=1}^{\chi} \lambda_\gamma^2 \ln \lambda_\gamma^2$ is small. We saw earlier that the maximum entanglement entropy of a reduced density matrix of size χ is $\ln \chi$. Thus one can estimate that one may need matrices of up to order $\chi_{\max} \sim e^{S_A}$ for a good representation of a state. In 1D, the border of two subsystem A and B is just a point. All entanglement between A and B must go through this point. One can show that for the ground state of gapped Hamiltonians with local couplings one needs only about $\chi_{\max} \sim \xi$ where ξ is the maximum of the spatial correlation length and the size of the system. This is the reason why matrix product states work so well in one-dimensional physical systems. However, in general dimension D, $S_{\max} \sim L^{D-1}$, the so-called area-law, which implies that the matrix dimension will need to grow exponentially in more than 1D.

Expectation values of one-site operators

A big advantage of the MPS representation is that only a few local matrices are needed to calculate the effect of a local operator on the state (see below), or its expectation value. We will here look at the expectation value of a one-site operator $\hat{O}^{[j]}$ that acts only on the spin at site j, for example $\hat{S}_z^{[j]}$, whose matrix representation is the third Pauli matrix. Its expectation value is
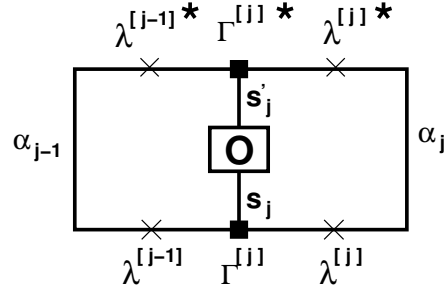
$$\langle \Psi | \hat{O}^{[j]} | \Psi \rangle = \sum_{\{s\},\{s'\}} \langle s_1' \dots s_L' | \dots \lambda^{*[j]} \Gamma^{*[j]s_j'} \lambda^{*[j-1]} \dots O^{[j]}_{s_j s_j'} \dots \lambda^{[j-1]} \Gamma^{[j]s_j} \lambda^{[j]} \dots | s_1 \dots s_L \rangle \tag{27}$$

In graphical representation, this becomes

At the interior vertical lines, the spins s_i' from the bra vector $\langle\psi|$ and s_i from the ket vector $|\psi\rangle$ meet. Since $\langle s_i'|s_i\rangle = \delta_{s_i s_i'}$, they have to be equal, except at the location j of the operator $\hat{O}^{[j]}$. Note that all lambda values are actually real, since they are singular values.

This expression can now be simplified by using the normalization Eqs. (24), which iteratively cause all matrices from both ends of the chain up to site j to just contribute Kronecker deltas. The remaining contribution is, in graphical representation

With $M_{\alpha_{j-1}\alpha_j}^{s_j} := \lambda_\alpha^{[j-1]} \, \Gamma_{\alpha_{j-1}\alpha_j}^{[j] \, s_j} \, \lambda_{\alpha_j}^{[j]}$ this becomes

$$\langle\psi|\hat{O}^{[j]}|\psi\rangle = \sum_{s,s'}\langle s'|\,\hat{O}\,|s\rangle \ \mathrm{tr}\big(M^{s'}\big)^\dagger M^s. \tag{28}$$

2.3 Time evolution

The time evolution of a state in the Schrödinger picture for a time-independent Hamiltonian is given by $|\Psi(t)\rangle = e^{-i\hat{H}t}|\Psi(0)\rangle$. We will discuss the case of Hamiltonians with local or nearest neighbor interactions, like in (2).

2.3.1 Trotter Suzuki decomposition

The difficulty now is that the Hamiltonians of adjacent sites do not commute, $[\hat{H}_i, \hat{H}_{i+1}] \neq 0$ and as a consequence the exponential $e^{-i\hat{H}t}$ cannot be expressed as a product of local operators $e^{-i\hat{H}t} \neq \prod_j e^{-i\hat{H}_j t}$. But the Hamiltonians of next nearest neighbor sites do commute: $[\hat{H}_i, \hat{H}_{i+2}] = 0$. It is thus helpful to decompose $\hat{H}$ into a sum of even and odd site Hamiltonians

$$\hat{H} = \hat{H}_{\mathrm{even}} + \hat{H}_{\mathrm{odd}} = \sum_{j,\mathrm{odd}} \hat{H}_j + \sum_{j,\mathrm{even}} \hat{H}_j \tag{29}$$

such that

$$e^{-i\hat{H}_{\mathrm{even}} t} = \prod_{j,even} e^{-i\hat{H}_j t} \quad \text{and} \quad e^{-i\hat{H}_{\mathrm{odd}} t} = \prod_{j,odd} e^{-i\hat{H}_j t}. \tag{30}$$

Within $\hat{H}_{\text{even}}$, all terms commute, and also within H_{odd}, but $[\hat{H}_{\text{even}}, \hat{H}_{\text{odd}}] \neq 0$. Next we subdivide the time t into small "time slices" of length Δt

$$e^{-i\hat{H}t} = \left(e^{-i\hat{H}\Delta t}\right)^{\frac{t}{\Delta t}} = \left(e^{-i(\hat{H}_{\text{even}}+\hat{H}_{\text{odd}})\Delta t}\right)^{\frac{t}{\Delta t}}.$$

Now we use the Baker-Hausdorff formula to get

$$e^{-i\hat{H}t} = \left(e^{-i\hat{H}_{\text{even}}\Delta t}\, e^{-i\hat{H}_{\text{odd}}\Delta t}\left(1 + \mathcal{O}\left((\Delta t)^2[\hat{H}_{\text{even}}, \hat{H}_{\text{odd}}]\right)\right)\right)^{\frac{t}{\Delta t}}.$$

Writing this product of $t/\Delta t$ terms explicitly yields

$$e^{-i\hat{H}t} = \left(e^{-i\hat{H}_{\text{even}}\Delta t}\, e^{-i\hat{H}_{\text{odd}}\Delta t}\, e^{-i\hat{H}_{\text{even}}\Delta t} \ldots e^{-i\hat{H}_{\text{even}}\Delta t}\right)\left(1 + \mathcal{O}(\Delta t)\right). \tag{31}$$

We lost one order of Δt because of the $(t/\Delta t)$ many factors. The Trotter-Suzuki decomposition leads to a series of operators $e^{-i\hat{H}_j t}$ which only act on two adjacent sites at once. The time evolution of the system is traced back to application of these 2-site operators. This strategy was introduced in the context of quantum Monte Carlo by Suzuki. It is also used for several popular MPS time evolution methods.

The smaller the time step Δt, the smaller the error in the method. One can gain another order of Δt with almost no effort by the *2nd order Trotter Suzuki approximation*

$$\mathrm{e}^{-i\hat{H}\Delta t} = \mathrm{e}^{-i\hat{H}_{\text{even}}\Delta t/2}\, \mathrm{e}^{-i\hat{H}_{\text{odd}}\Delta t}\, \mathrm{e}^{-i\hat{H}_{\text{even}}\Delta t/2} + \mathcal{O}\left((\Delta t)^3\right). \tag{32}$$

For the time evolution of a state $|\Psi\rangle$ this requires no more effort than the first order approximation, because $\mathrm{e}^{-i\hat{H}_{\text{even}}\Delta t/2}\, \mathrm{e}^{-i\hat{H}_{\text{even}}\Delta t/2} = \mathrm{e}^{-i\hat{H}_{\text{even}}\Delta t}$. The only difference occurs when measurements are performed: for the 2nd order approximation, measurements have to be performed after *half*-time-steps $\mathrm{e}^{-i\hat{H}_{\text{even}}\Delta t/2}$.
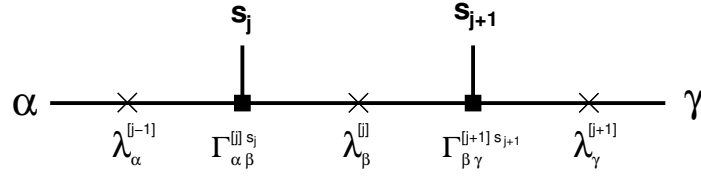
2.3.2 Application of 2-site operators

In order to calculate the time evolution, we need to apply the 2-site operators $\hat{H}_i$ to $|\Psi\rangle$. For a general 2-site operator, we want to calculate

$$|\Psi'\rangle = \hat{O}^{[j,j+1]}|\Psi\rangle. \tag{33}$$

The structure of MPS as products of matrices located on individual sites is again very helpful. Since $\hat{O}^{[j,j+1]}$ acts on sites j and $j + 1$, only the Γ-matrices at these sites and the λ-matrix in *between* are affected, but not the outer λ-matrices containing the entanglement with the environment. Let χ be the dimension of all these matrices. The calculations turn out to be easier when one also includes the two outer λ-matrices. We therefore look at the part of the MPS shown in Fig. 4. This object has spin indices s_j, s_{j+1} on which the operator will act, and free matrix indices α and γ. It is the graphical representation of

$$\psi_{\alpha\gamma}^{s_j\, s_{j+1}} := \sum_{\beta} \lambda_{\alpha}^{[j-1]}\, \Gamma_{\alpha\beta}^{[j]\, s_j}\, \lambda_{\beta}^{[j]}\, \Gamma_{\beta\gamma}^{[j+1]\, s_{j+1}}\, \lambda_{\gamma}^{[j+1]}. \tag{34}$$

Fig. 4: *The coefficients $\psi_{\alpha\gamma}^{s_j\,s_{j+1}}$ of an MPS affected by two-site operators.*

In the context of DMRG, it is called the wave-function. The application of $\hat{O}$ on ψ yields

$$\tilde{\psi}_{\alpha\gamma}^{s'_j\,s'_{j+1}} := \sum_{s_j,s_{j+1}} \langle s'_j\,s'_{j+1}|\,\hat{O}\,|s_j\,s_{j+1}\rangle\,\psi_{\alpha\gamma}^{s_j\,s_{j+1}}. \tag{35}$$

We want to express $|\Psi'\rangle$ as a normalized MPS, similar to $|\Psi\rangle$. We therefore need to write $\tilde{\psi}$ in the same form as the original ψ, with new normalized matrices $\tilde{\Gamma}_{\alpha\beta}^{[j]s'_j}$, λ_β, and $\tilde{\Gamma}_{\beta\gamma}^{[j+1]s'_{j+1}}$.
In order to get there, we first interpret $\tilde{\psi}$ as a matrix with two indices, a row index $(\alpha s'_j)$ and a column index $(\gamma s'_{j+1})$

$$\bar{\psi}_{(\alpha s'_j),(\gamma s'_{j+1})} := \tilde{\psi}_{\alpha\gamma}^{s'_j\,s'_{j+1}}. \tag{36}$$

Next we perform an SVD on $\bar{\psi}$

$$\bar{\psi}_{(\alpha s'_j),(\gamma s'_{j+1})} = \sum_{\beta=1}^{2\chi} U_{(\alpha s'_j)\beta}\,\tilde{\lambda}_\beta\,V_{\beta(\gamma s'_{j+1})}^\dagger. \tag{37}$$

Note that U is the unchanged $\lambda^{[j-1]}$ times a new $\Gamma^{[j]}$ and is equivalent to a new A-matrix, and $V^\dagger$ is a new $\Gamma^{[j+1]}$ times the unchanged $\lambda^{[j+1]}$, equivalent to a new B-matrix.
Because of the presence of s'_j and s'_{j+1} in the indices (with 2 values $\uparrow,\downarrow$), this SVD has a Schmidt rank up to *twice the rank* of the original matrices Γ,λ. If we kept this increased rank, then the matrix dimensions would explode exponentially during the time evolution. We therefore need to *truncate* the matrix dimensions, for example back to the original χ, by discarding the smallest singular values in $\tilde{\lambda}$. We then need to calculate the discarded weight t_w and re-normalize $\tilde{\lambda}_\beta \rightarrow \tilde{\lambda}_\beta / \sqrt{1-t_w}$. The matrices U and $V^\dagger$ are also truncated at the new size.
In the so-called **tebd** algorithm [34, 35], which works in the canonical representation, new Γ-matrices are then extracted, by splitting the *unchanged* outer matrices $\lambda^{[j-1]}$ and $\lambda^{[j]}$ off U and $V^\dagger$, by means of applying the pseudoinverse:

$$\tilde{\Gamma}_{\alpha\beta}^{[j]s'_j} = (\lambda_\alpha^{[j-1]})^{\text{inv}}\,U_{(\alpha s'_j)\beta} \;, \quad \tilde{\Gamma}_{\beta\gamma}^{[j+1]s'_{j+1}} = V_{\beta(\gamma s'_{j+1})}^\dagger\,(\lambda_\gamma^{[j+1]})^{\text{inv}}. \tag{38}$$

As desired, this results in updated $\chi \times \chi$ matrices $\tilde{\Gamma}_{\alpha\beta}^{[j]s'_j}$, $\tilde{\lambda}_\beta$, and $\tilde{\Gamma}_{\beta\gamma}^{[j+1]s'_{j+1}}$. This method has the disadvantage of potential instabilities from the divisions. They can also be avoided [7].
A different valid time-evolution with similarly small Trotter error, which is not commonly used but will be employed in the FTPS method, does not step by two sites in even/odd fashion, but **steps only by one site**, using $\tilde{\lambda}^{[j]}V^{[j+1]\dagger}$ from Eq. (37) multiplied from the right with $\Gamma^{[j+2]}\lambda^{[j+2]}$ as the next $\psi^{s_{j+1}\,s_{j+2}}$ to be updated.

A mathematical equivalent of tebd is the **t-DMRG** algorithm [36, 37], which works in the mixed-canonical representation, i.e., with only A and B matrices, and with the even/odd Trotter split. When moving from the left to the right, the U matrix from the SVD defines the matrix $A^{[j]}$ of the updated state. In order to step another site to the right, $\psi^{s_{j+1} s_{j+2}}$ introduced in the previous paragraph is subjected to another SVD: $\psi = UDV^\dagger$, which yields $A^{[j+1]}$ from U, while D should be the unchanged $\lambda^{[j+1]}$ and $V^\dagger$ the unchanged $\Gamma^{[j+2]}\lambda^{[j+2]}$. Multiplying $DV^\dagger$ from the right by the next B-matrix $(=\Gamma^{[j+3]}\lambda^{[j+3]})$ provides the next wave function ψ in t-DMRG, at the disadvantage of an additional SVD operation.

Another possibility for time evolution is by way of repeated application of the complete Hamiltonian to the state, in the simplest case as $(1 + H\Delta t)^{t/(\Delta t)}$. The complete Hamiltonian can be applied as a so-called Matrix-Product Operator (**MPO**), to be discussed next.

Swap gate

A swap gate switches the physical role of two neighboring sites in an MPS [38, 7]. It amounts to applying the two-site operator

$$S_{ij} = \delta_{s_i, s'_j} \, \delta_{s_j, s'_i} \, (-1)^{n_i n_j} \tag{39}$$

to a state with physical indices s_i, s_j. The sign factor provides for fermion anticommutation.

2.4   Matrix product operators (MPO) and DMRG

In the same way as the coefficients of a state can be expressed as a product of matrices in Eq. (4) this can also be done for the coefficients of a many-particle operator $\hat{O}$ in terms of matrices $W^{[s_i, s'_i]}_{\alpha_{i-1}\alpha_i}$

$$\hat{O} = \sum_{\{s_i\},\{s'_i\}} W^{s_1, s'_1} W^{s_2, s'_2} \dots W^{s_L, s'_L} |s'_1, s'_2, \dots, s'_L\rangle\langle s_1, s_2, \dots, s_L| , \tag{40}$$
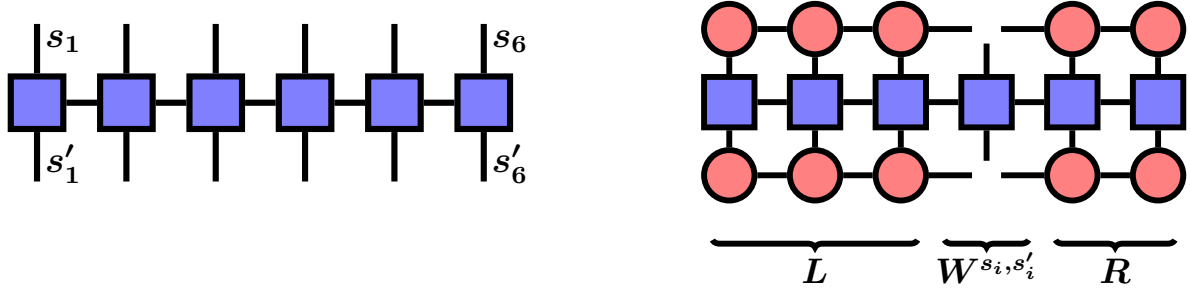
where the internal matrix indices α_i have been omitted. The graphical representation of this MPO is shown in Fig. 5. Methods for obtaining the W-matrices can, e.g., be found in Ref. [7]. For a simple Anderson impurity model, they will be shown explicitly below.

2.4.1   DMRG ground state search

The DMRG method [8, 7] optimizes the energy of a state $|\psi\rangle$ site by site (or in pairs of sites) in order to find the state with minimum energy. Here we just provide a brief idea of the method. It works in the mixed canonical representation. Each optimization of a local MPS matrix $A^{[i]}$ can be formulated as a linear equation

$$H^{\text{eff}}_i A^{[i]} = \lambda \, A^{[i]}, \tag{41}$$

for which the matrix with the lowest eigenvalue λ needs to be found, for example with a Lanczos method. The effective Hamiltonian H^{eff} is most easily expressed in graphical form, as in Fig. 5.

Fig. 5: *Left: graphical representation of a matrix product operator. The disconnected lines symbolize again physical degrees of freedom s_i. The operator connects to an MPS with the lower indices, which implies a summation over $\{s_i\}$, producing a new MPS with indices $\{s_i'\}$. Right: Effective Hamiltonian for DMRG. It is applied to an MPS matrix $A^{[s_i]}_{\alpha_{i-1}\alpha_i}$ on the bottom, producing an effective A-matrix on the top, which has to satisfy Eq. (41).*

This local minimization works amazingly well, as mentioned earlier. Sometimes it can, however, get stuck in local minima. Because of the limited amount of entanglement available in an MPS, DMRG tends, for example, to converge to an ordered state, like, e.g., a Néel state in case of an antiferromagnet. Care must be taken to either avoid this or to correctly interpret the resulting state.
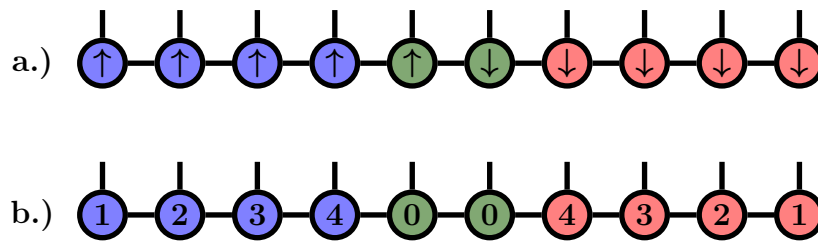
2.4.2 MPO representation of an Anderson impurity model Hamiltonian

Let us now explicitly discuss an MPO which represents an Anderson impurity model Hamiltonian. More details can be found in Ref. [9]. To keep indices manageable, we will first discuss the standard AIM with a single orbital

$$H = \sum_{k\sigma} \varepsilon_k \, n_{k\sigma} + \sum_{k\sigma} V_k \big(c^{\dagger}_{0\sigma} c_{k\sigma} + h.c. \big) + \sum_{\sigma} \varepsilon_0 \, n_{0\sigma} + U \, n_{0\uparrow} n_{0\downarrow}. \tag{42}$$

We number sites like in Fig. 6. We will need MPOs of internal dimension 4 in order to code the four terms in H. For the leftmost site, the W-tensor of the MPO is a vector in internal MPO space. (This space is denoted by the horizontal indices in Fig. 5.) The physical indices are not written explicitly in the equations below; they are implied by the operators.

$$W_{1\uparrow} = \big(\varepsilon_1 \, n_{1\uparrow} \quad \mathbb{1} \quad V_1 c_{1\uparrow} \quad V_1 c^{\dagger}_{1\uparrow} \big) \tag{43}$$

Fig. 6: *Numbering of sites for a single orbital Anderson impurity model. Here the number of bath sites for each spin is $N_B = 4$.*

Each following site of the left bath gets

$$W_{k\uparrow} = \begin{pmatrix} \mathbb{1} & 0 & 0 & 0 \\ \varepsilon_k n_{k\uparrow} & \mathbb{1} & V_k c_{k\uparrow} & V_k c_{k\uparrow}^\dagger \\ 0 & 0 & p & 0 \\ 0 & 0 & 0 & p \end{pmatrix} \tag{44}$$

as a W-tensor. The operator $p = (-1)^n$ provides for a Jordan-Wigner transformation, i.e., it ensures fermionic commutation rules. Now

$$\prod_{k=1}^{N_b} W_{k\uparrow} = \begin{pmatrix} \sum_{k=1}^{N_b} \varepsilon_k n_{k\uparrow} & \mathbb{1} & \sum_{k=1}^{N_b} V_k c_{k\uparrow} & \sum_{k=1}^{N_b} V_k c_{k\uparrow}^\dagger \end{pmatrix} \tag{45}$$

(with the p operators omitted in the last equation).

W-tensors for the spin-down chain are equivalent, but with transposed matrices, and a column instead of a vector for the rightmost MPO. Finally, the W-tensors for the impurity sites are

$$W_{0\uparrow} = \begin{pmatrix} 0 & \mathbb{1} & 0 \\ \mathbb{1} & \varepsilon_0 n_{0\uparrow} & n_{0\uparrow} \\ 0 & c_{0\uparrow}^\dagger & 0 \\ 0 & c_{0\uparrow} & 0 \end{pmatrix}, \quad W_{0\downarrow} = \begin{pmatrix} \mathbb{1} & \varepsilon_0 n_{0\downarrow} & c_{0\downarrow}^\dagger & c_{0\downarrow} \\ 0 & \mathbb{1} & 0 & 0 \\ 0 & U n_{0\downarrow} & 0 & 0 \end{pmatrix}. \tag{46}$$

Multiplying all these matrices together produces the desired Hamiltonian Eq. (42).

2.5   Previous MPS impurity solvers

As spelled out in the introduction, we need to calculate the ground state of an Anderson Impurity Model (AIM), apply a creation or annihilation operator, and time evolve. In order to do this efficiently with MPS, where the computational effort for matrix dimension m grows like m^3, we need small matrices and few physical degrees of freedom per site. For a single spinful orbital, it turns out that it is best to split spin-up and spin-down into the chain geometry of Fig. 6 (top). Using real-time evolution, this allows for a very precise impurity solver, with large baths (easily $\mathcal{O}(100)$ and more) and with excellent energy resolution in DMFT [31]. With two orbitals, a successful strategy has been to split the *orbitals* into two separate chains, which also provided a precise impurity solver [31]. An advantage of this geometry is that the spins of each orbital, which are likely to be entangled, are located together. However, now the local Hilbert space at each MPS site has doubled, from two states (occupied, unoccupied) to the four states of a spinful orbital. Unfortunately this *squares* the computational effort. With a geometry like in Fig. 6, the computational effort will grow like

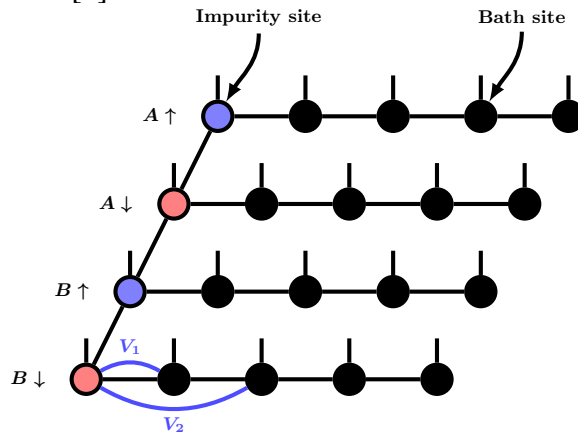$$\text{computational effort} \sim m^{3 \times n_{\text{orbital}}}. \tag{47}$$

More than two orbitals have turned out to be infeasible with this geometry, and the MPS approach to impurity solvers was stuck at this stage for a while.

3 Fork tensor product state (FTPS) method

3.1 Geometry and tensors

The key ingredient of the new FTPS method is the geometry of Fig. 7. This is a special case of a so-called Tree Tensor Network. For a 2-orbital NRG calculation such a geometry was also employed in Ref. [39]. Each bath chain has a fixed spin and orbital, i.e., the local Hilbert space dimension in the bath is only two (occupied/unoccupied). In addition, the interacting impurity site is also split up into a chain of FTPS sites with dimension two (single orbital of fixed spin). An apparent disadvantage of the FTPS geometry seems to be that entanglement between bath sites of different spin or different orbitals has to be transported by the encoding matrices over a large distance, so that each bond may have to carry a lot of entanglement. This is however similar to the situation in Fig. 6 and turns out not to be a big problem on the bonds between the bath sites. The actual bottleneck in this approach is the entanglement on the vertical bonds in the figure, between the sites representing the impurity, which must contain the entanglement between the baths as well as additional large entanglement from the interaction between the impurity degrees of freedom. As we will see, the computational effort for precise calculations will still remain reasonable.

The FTPS sites for the impurity (like $B_\uparrow$) now each contain a *tensor* with three instead of two bond indices, and one physical index, like $I^s_{\alpha\beta\gamma}$. Because of the geometric tree structure, a cut through any bond still bipartitions the system into two subsystems. Therefore one can still obtain a Schmidt decomposition. In the case of MPS, we needed to combine one bond index α with a physical index s of an MPS "matrix" $A^s_{\alpha\beta}$ in order to obtain an matrix $A_{(\alpha s),\beta}$ to which an SVD can be applied. For FTPS, we need to combine the indices of the impurity tensors. To get an idea of the computational effort, suppose that the impurity bond dimensions are m, the bath bond dimension at the impurity is n, and the physical Hilbert space dimension is $d(=2)$. Then the size of the matrix is $m\,n\,d \times m$ and the computational effort for the SVD will be $\mathcal{O}(m^3\,n\,d)$. For all bipartitions, one can also obtain properly normalized states, and therefore apply all the usual MPS and DMRG algorithms. Note that off-diagonal hybridizations can in principle be incorporated into the method [5].

Fig. 7: *Tensor geometry of the Anderson impurity model for the FTPS method, drawn for two orbitals A and B. Further orbitals can be incorporated with additional bath chains. From [5].*

3.2   Star representation of the bath orbitals

A second ingredient of FTPS is a special encoding of the bath. Usually, the bath has been represented in MPS approaches as a tight binding Wilson chain, which can be obtained from Eq. (1) by a basis transformation. The Wilson chain appears natural for MPS since it is a one-dimensional physical system with only nearest neighbor hopping and local energies for occupied sites. It was shown by Wolf *et al.* [40], that, quite surprisingly, it can be better to use the original bath sites k of Eq. (1) sequentially as the sites of a bath chain. This so-called *star geometry* (see Fig. 1) is also used in FTPS. One can, for example, number the sites by increasing local energy ε_k. The advantage is that sites with low ε_k will be almost completely occupied, and sites with large ε_k almost completely unoccupied, so that they do not contribute much to the entanglement. Only sites with intermediate ε_k will have sizeable contributions from both occupied and unoccupied basis states and therefore contribute to the entanglement. Wolf *et al.* [40] showed that the maximum matrix dimension necessary in star geometry can be considerably lower than in the Wilson chain representation.

The disadvantage of the star geometry comes from artificially putting it on a chain of sites in order to apply the MPS formalism. Each bath site interacts with the impurity, by the hopping strength V_k, but not with its neighbors. We thus have many *non-local* couplings, from each bath site to the impurity, which are usually difficult and expensive for MPS approaches. Wolf *et al.* [40] treated the nonlocal hopping with a Krylov based [41] method.

We will instead use successive *swap* operations which effectively transport the impurity site (like $B_\uparrow$) along its chain, and later back, so that interactions become local. Details will be described below. It turns out that this approach, together with a specific Trotter breakup, has a very small error in time evolution, which is more than an order of magnitude better than with the Wilson chain representation for similar computational effort.

3.3   Kanamori Hamiltonian and FTPOs

In the results section, we will treat the multi-orbital Kanamori Hamiltonian

$$H = H_{\text{loc}} + H_{\text{bath}} \tag{48}$$

$$H_{\text{loc}} = \varepsilon_0 \sum_{m\sigma} n_{m0\sigma} + H_{\text{DD}} + H_{\text{SF}} + H_{\text{PH}}$$

$$H_{\text{DD}} = U \sum_m n_{m0\uparrow} n_{m0\downarrow} + (U - 2J) \sum_{m'>m,\sigma} n_{m0\sigma} n_{m'0\bar{\sigma}} + (U - 3J) \sum_{m'>m,\sigma} n_{m0\sigma} n_{m'0\sigma}$$

$$H_{\text{SF}} = J \sum_{m'>m} \left(c^\dagger_{m0\uparrow} c_{m0\downarrow} c_{m'0\uparrow} c^\dagger_{m'0\downarrow} + \text{h.c.} \right)$$

$$H_{\text{PH}} = -J \sum_{m'>m} \left(c^\dagger_{m0\uparrow} c^\dagger_{m0\downarrow} c_{m'0\uparrow} c_{m'0\downarrow} + \text{h.c.} \right)$$

$$H_{\text{bath}} = \sum_{ml\sigma} \varepsilon_l n_{ml\sigma} + V_l \left(c^\dagger_{m0\sigma} c_{ml\sigma} + \text{h.c.} \right),$$

where m numbers the orbitals.

H_{DD} contains density interactions and H_{SF} and H_{PH} incorporate spin-flip and pair-hopping terms. For our FTPS geometry, the MPOs ("Matrix Product Operators") now become FTPOs ("Fork Tensor Product Operators") with tensors in the same geometry as the FTPS in Fig. 7. For the bath, the W-tensors are very similar to the single orbital case. For the impurities, one needs tensors with two or three auxiliary indices for the connections in the fork structure, and two physical indices. Since the Kanamori Hamiltonian contains more terms than the simple AIM Hamiltonian in Eq. (42), the W-tensors become much larger, up to $8 \times 13 \times 4$, with 4 corresponding to the MPO dimension of the bath tensors, Eq. (45), for one bath chain. Details can be found in Ref. [9].

3.4 Ground state and time evolution

Ground state

Given the FTPO representation of the Kanamori Hamiltonian and the tree geometry which assures a bipartition of the system at every bond, the ground state can now be calculated by the DMRG method. For FTPS, this takes a considerable amount of computer time, and care needs to be taken that the true ground state is reached.

The most expensive parts of the calculation are SVDs. For the bath chains this is relatively inexpensive, since they have the structure of an MPS and the entanglement in the chains is relatively small in practice. The most expensive part is in the optimization of the impurity tensors and the accompanying SVDs. When the bonds between impurity tensors have dimension m and the bonds from the last bath tensor to the corresponding impurity tensor has dimension n, the cost for two-site DMRG will scale like $\mathcal{O}(mnd)^3$, where $d = 2$ is the physical dimension.

Time evolution of the FTPS

The time evolution operator for a small time step can be decomposed by repeated application of the second order Suzuki Trotter approximation into [5]

$$e^{-i\Delta t H} \approx \prod_{m'>m} e^{-i\frac{\Delta t}{2}(H_{\mathrm{SF}m,m'}+H_{\mathrm{PH}m,m'})} \; e^{-i\frac{\Delta t}{2}H_{\mathrm{DD}}} \; e^{-i\Delta t H_{\mathrm{free}}} \; e^{-i\frac{\Delta t}{2}H_{\mathrm{DD}}} \prod_{m'>m} e^{-i\frac{\Delta t}{2}(H_{\mathrm{SF}m,m'}+H_{\mathrm{PH}m,m'})},$$

(49)

where $H_{\mathrm{free}} = H_{\mathrm{bath}} + \varepsilon_0 \sum_{m\sigma} n_{m0\sigma}$. Note that H_{SF} and H_{PH} commute with each other, but not with H_{DD}. The time evolution operators for H_{DD}, H_{SF}, and H_{PH} can each be written as an FTPO, i.e., an operator acting on the impurity tensors in the FTPS: H_{DD} does not change particle numbers. Therefore fermion anticommutation plays no role and the FTPO for $e^{-i\Delta t H_{\mathrm{DD}}}$ can be constructed by exponentiating the $4^{N_{\mathrm{orb}}} \times 4^{N_{\mathrm{orb}}}$ matrix of H_{DD} and then bringing it into FTPO-form (i.e. a product of local tensors) by repeated SVDs.

H_{SF} and H_{PH} do move fermions between orbitals, so that the fermion sign needs to be treated. Both cases can be simplified in the same way because $\hat{A}^3 = \hat{A}$ for $J\hat{A} = H_{\mathrm{SF}}$ and for $-J\hat{A} = H_{\mathrm{PH}}$. Then

$$e^{-i\Delta t J\hat{A}} = \mathbb{1} + \hat{A}^2\Big(\cos(\Delta t J) - 1\Big) - i\hat{A}\sin(\Delta t J).$$

(50)

FTPOs for $\hat{A}$ and $\hat{A}^2$ with the correct fermion signs can be constructed directly. With respect to bond indices connecting impurity orbitals, they become sparsely populated matrices of sizes up to 6×10 [9]. To perform time evolution with, e.g., $e^{-i\Delta t H_{\mathrm{DD}}}$, one applies the corresponding FTPO and subsequently brings the state back into normalized form. This leaves the time evolution with H_{free} to be performed. Since in Eq. (48) there are no terms connecting different baths, it decomposes directly into separate time evolutions for each bath chain.

Time evolution of a bath chain in star representation

As mentioned above, we choose the star representation for the baths. In Ref. [40], the time evolution was done by a Krylov technique, which involves multiple applications of the MPO for H_{free} constructed in section 2.4. In the best case, up to two orders of magnitude were saved in CPU time vs. a Wilson chain calculation. In our FTPO method we use a different technique based on a Trotter expansion. A comparison between different techniques for the star geometry has not yet been performed.

Each chain (m, σ) is evolved independently. For ease of notation, we leave out the orbital and spin indices m and σ and now number the sites from left to right as 0 (impurity), $1, 2, 3, \ldots, N_B$ (cf. Eq. (51)). Defining $V_0 = 0$ we can write $H_{\mathrm{free}} = \sum_{l=0}^{N_B} H_l$ with $H_l = \varepsilon_l n_l + V_l \left(c_0^\dagger c_l + \mathrm{h.c.} \right)$ and use the second order Trotter expansion $e^{-i\Delta t H_{\mathrm{free}}} = e^{-i\frac{\Delta t}{2} H_0} e^{-i\Delta t \sum_{l=1}^{N_B} H_l} e^{-i\frac{\Delta t}{2} H_0} + \mathcal{O}(\Delta t^3)$, which after iteration becomes
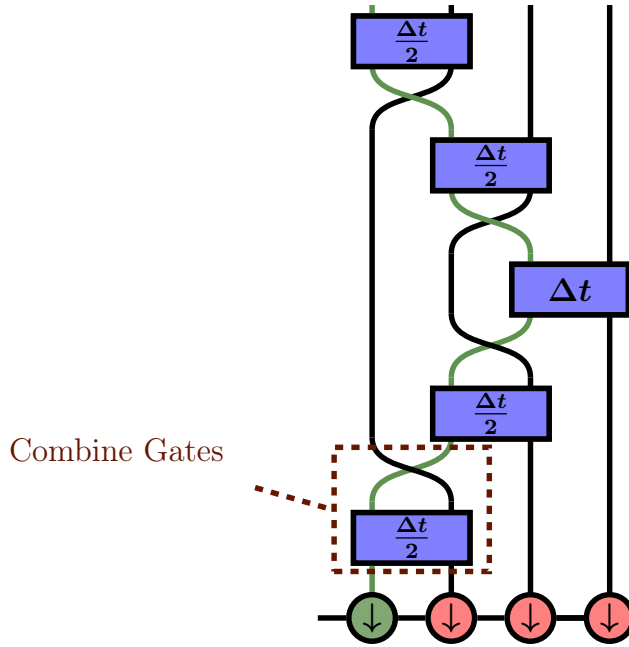
$$e^{-i\Delta t H_{\mathrm{free}}} = \prod_{l=0}^{N_B} e^{-i\frac{\Delta t}{2} H_0} \prod_{l=N_B}^{0} e^{-i\frac{\Delta t}{2} H_0} + \mathcal{O}(\Delta t^3). \tag{51}$$

At first glance this looks just like a first order Trotter expansion with two time steps of size $\Delta t/2$, but due to the reversed order in the second part, the expansion is in fact of second order. Eq. (51) still contains long-range hopping. We solve this problem by use of swap gates: First apply the nearest neighbor two-site operator $e^{-i\frac{\Delta t}{2} H_0}$ which connects an impurity site and the first bath site and subsequently *swap* these two sites. These two operations can be combined into a single two-site gate, so that no additional SVD is necessary. Now the impurity is located between bath sites 1 and 2 and we can apply $e^{-i\frac{\Delta t}{2} H_1}$ followed by another swap of the impurity to the right, and so on. The procedure is graphically depicted in Fig. 8. After reaching the last bath site on the right, the time evolutions continue to the left, following Eq. (51) until at the end the impurity site is back at its original location.

We find [42] that this time evolution in star geometry produces results which are more than an order of magnitude more precise than results with a Wilson chain geometry. Furthermore, indirectly due to the almost diagonal nature of Eq. (42), the error does almost *not* grow with bath size N_B, differently from what would have been expected naively from Eq. (51).

This completes the steps listed in section 1.2 for the impurity solver, i.e., for calculating the spectral function $A(\omega)$, which can then be fed into the DMFT iteration to obtain an improved bath spectral function, until the DMFT loop converges.

Fig. 8: *Sequence of time evolution gates for the bath.*

4 Results

In order to provide an impression of the possibilities and limitations of the real time FTPS solver, we will consider some examples. Further details can be found in Refs. [5,6]. Before we go to DMFT spectra, let us first look at the parameters involved in an FTPS calculation, and at related checks of correctness, robustness, and convergence.

Correctness. The solver and its implementation was checked by comparison to exact solutions of small interacting and large non-interacting systems, as well as by comparison to results of an earlier one- and two-orbital MPS solver [31], which itself had been thoroughly verified.

Bath size. FTPS work on a discretized bath representing the hybridization function $\Delta(\omega)$, with completely flexible discretization. It becomes more precise when the number N_B of sites in the bath chains is increased, which is quite inexpensive to do because the MPS calculations on the bath in star geometry are very efficient (in contrast to, e.g., Exact Diagonalization). Baths of $\mathcal{O}(100)$ sites per orbital and spin can be treated and the results shown are converged in N_B up to some small variations [5,6].

Matrix dimension and truncated weight. The numerical approximation in MPS/FTPS methods is in the finite bond dimension achievable ($\mathcal{O}(100) - \mathcal{O}(1000)$), associated with a truncated weight t_W, usually of the order of 10^{-8}. Convergence of results was verified in Ref. [5].
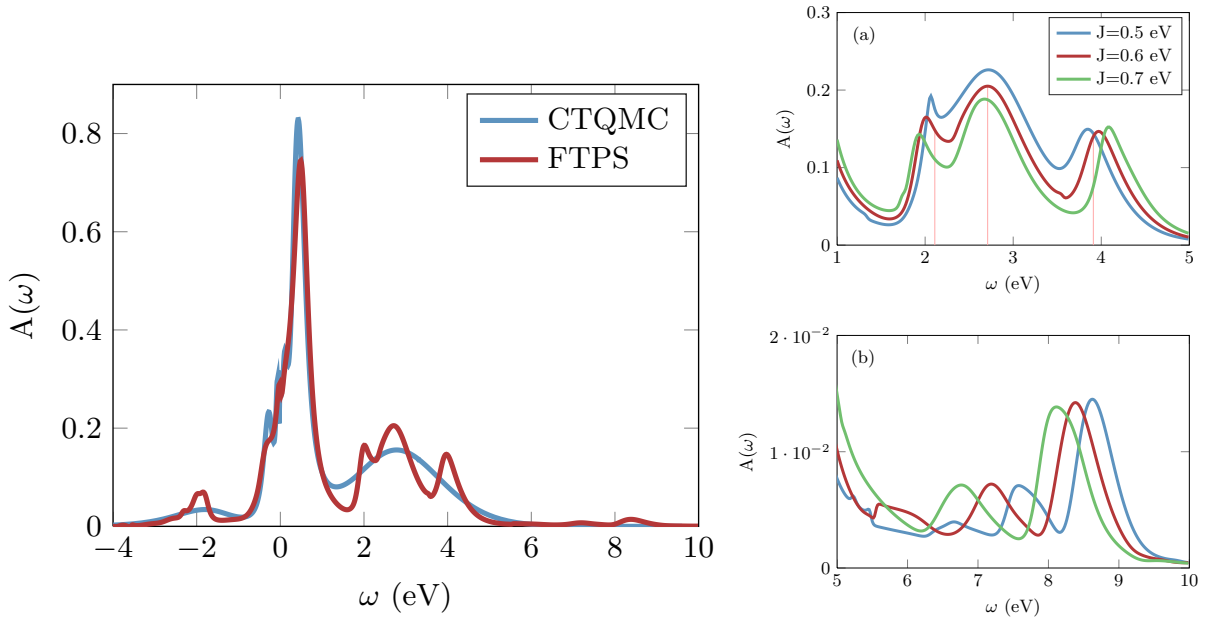
Time evolution. Time evolution is done in finite steps, e.g., $\Delta t = 0.01$ eV, small enough so that the associated Trotter errors are not important. However, during time evolution, the entanglement increases, making larger matrices necessary, and eventually limiting the maximum time which can be reached reliably. Fortunately, the Green function $G(t)$ only involves a local excitation from the ground state at the impurity, for which entanglement growth is quite slow. In the examples below, time evolution was done both forward and backward in time [43] and

typical total times reached were 16 eV^{-1}. The finite maximum time puts some limit on the energy resolution. This can be improved by so-called „linear prediction" [27, 7, 31] of the time series, which is badly named and actually amounts to a clever way of describing the spectrum with $\mathcal{O}(100)$ or more Lorentzians. The reliability of this procedure for a DMFT solver, including very sharp spectral features, was investigated in detail in [31]. In the FTPS calculations for SrVO$_3$, the extrapolation is, for example, done to 250 eV^{-1}. In order to avoid effects of the remaining cut-off and potential inaccuracies, the Fourier transform from $G(t)$ to $A(\omega)$ in these calculations was performed with a broadening of $\eta = 0.02$ eV. The full five-orbital calculations for SrMnO$_3$ were more demanding. A maximum bath size of $N_B = 49$ was used, during the DMFT loop a broadening of $\eta = 0.2$ eV, and for the final spectrum a broadening of only $\eta = 0.01$ eV in order to obtain optimal energy resolution.

4.1 SrVO$_3$: 3 orbitals

Fig. 9 shows DMFT spectra obtained with the FTPS solver [5] for the benchmark material SrVO$_3$ modeled by the Kanamori Hamiltonian with 3 orbitals, in comparison to results obtained by CTQMC at similar computational effort. Both spectra show a compatible central peak, an excitation below, and an upper Hubbard peak around 3 eV. However, the FTPS spectrum resolves much more detailed structure, especially within the upper Hubbard band, and even peaks around 8 eV. Both are missing in the CTQMC results. In Ref. [5] it is shown that this is due to the analytic continuation (by a standard Maximum Entropy technique) from the imaginary times/frequencies of the CTQMC to the real frequencies of the Green function. Indeed, when one transforms the FTPS Green function to imaginary frequency, it is compatible with the CTQMC Green function, which however has fairly large statistical errors. When one adds such noise to the FTPS Green function in imaginary frequency and transforms back to real frequency, the result is almost identical to the CTQMC spectrum, without structure in the upper Hubbard band and beyond.

At the central peak, FTPS is less precise than CTQMC, because very small frequencies correspond to very large times, which are less precisely calculated in FTPS. Conversely, high energies (small times) are *easiest* to resolve with FTPS. The structure of the spectrum in the upper Hubbard band contains interesting physics. In Ref. [5] it is shown that the peaks correspond directly to the excitations of the atomic model, i.e., the Kanamori Hamiltonian without bath, but shifted and broadened by the interaction with the bath. The atomic energies and corresponding states are shown in Table 1. From the positions of the peaks, one can thus extract couplings for an effective atomic model which would have peaks at the same positions (with some slight variations). The bare $U = 4$ eV becomes $U_{\text{eff}} = 5.97$ eV, $\varepsilon_0 = -0.86$ eV goes to $\varepsilon_{0,\text{eff}} = -2.00$ eV and the Hund's coupling becomes $J_{\text{eff}} = 0.59(6)$ eV, $0.66(3)$ eV, and $0.72(2)$ eV at bare couplings of 0.5 eV, 0.6 eV, and 0.7 eV, respectively. The amplitude of the peaks relates to their degeneracy in the atomic description. However, the detailed shape of the peaks is entirely due to the interaction with the bath and is not covered by this effective atomic model.

Fig. 9: *DMFT spectra for SrVO$_3$, at $U = 4$ eV and $J = 0.6$ eV, for a case without spin-flip and pair-hopping terms. With full rotational symmetry, i.e., including those terms, similar results are obtained. From Ref. [5].*
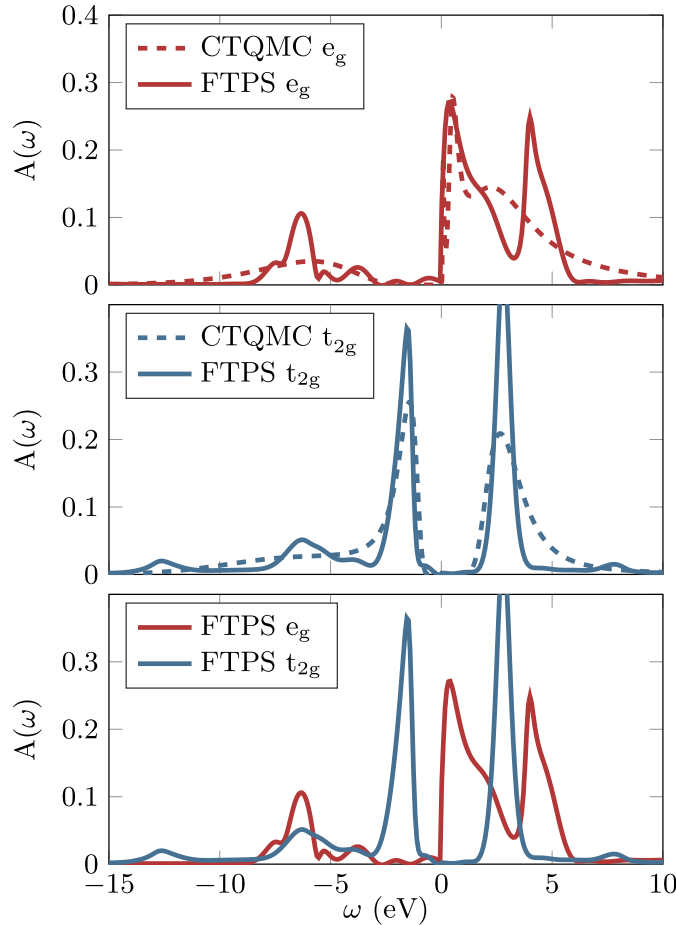
particle sector	atomic energy	degeneracy	state
0	ε_0	1	$|0, 0, 0\rangle$
1	0	6	$|\uparrow, 0, 0\rangle \ldots$
2	$U - 3J + \varepsilon_0$	6	$|\uparrow, \uparrow, 0\rangle \ldots$
	$U - 2J + \varepsilon_0$	6	$|\uparrow, \downarrow, 0\rangle \ldots$
	$U \quad\ + \varepsilon_0$	3	$|\uparrow\downarrow, 0, 0\rangle \ldots$
3	$3U - 9J + 2\varepsilon_0$	2	$|\uparrow, \uparrow, \uparrow\rangle \ldots$
	$3U - 5J + 2\varepsilon_0$	6	$|\uparrow, \uparrow, \downarrow\rangle \ldots$
	$3U - 7J + 2\varepsilon_0$	12	$|\uparrow\downarrow, \uparrow, 0\rangle \ldots$

Table 1: *States of the Kanamori Hamiltonian without spin-flip and pair-hopping terms.*

Amazingly, even the next set of excitations, around 8 eV, is resolved very well by the FTPS calculation, even though the amplitudes are very small. Again the individual peaks correspond to atomic excitations, however with somewhat different effective couplings. This set of peaks is entirely missing in the CTQMC results, likely because analytic continuation becomes extremely difficult at high energies.

4.2 SrMnO$_3$: 5 orbitals

Finally, we will briefly discuss results for a full five-orbital calculation with FTPS, for the material SrMnO$_3$. In Ref. [6], such calculations were used to examine the influence of different strategies for getting from a DFT spectrum to an effective Hamiltonian, specifically which orbitals and which range of energies of the DFT spectrum to include. It was shown that for SrMnO$_3$, it is important to use a wide energy range and to include the e_g orbitals. In the DFT spectrum (not shown), the e_g orbitals have are almost completely located above the Fermi en-
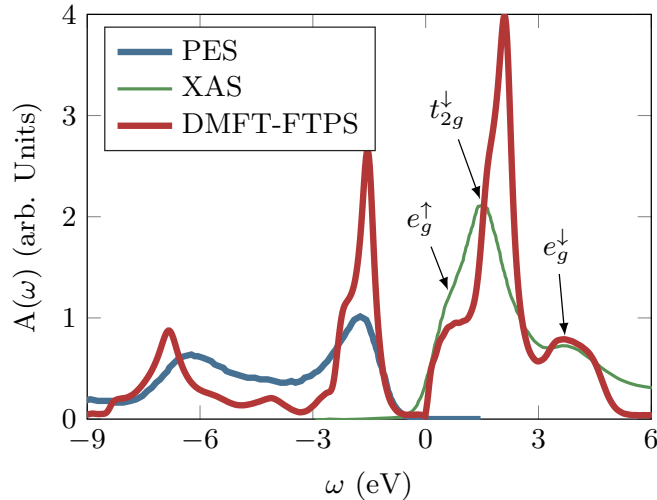
Fig. 10: *DMFT spectra for SrMnO$_3$ in a five orbital description, from FTPS calculations and from CTQMC. From [6].*

ergy. Fig. 10 shows DMFT spectra for five-orbital calculations with a wide energy window. The FTPS spectra are compatible with the CTQMC but show considerably more detail. CTQMC is especially difficult for the e_g orbitals here because they are almost unoccupied, which makes the number of events for measuring the Green function in the Monte Carlo small.

From the combined spectrum in Fig. 10 (bottom) one sees that the size of the gap is in fact determined by the e_g contribution to the spectrum. Here one can also identify the e_g vs. t_{2g} nature of the successive peaks in the spectrum.

Fig. 11 compares the total FTPS DMFT spectrum to experimental results for the Mn-$3d$ orbitals in SrMnO$_3$ obtained by Kim *et al.* [44] with two different experimental techniques: photo emission spectroscopy (PES) below the Fermi energy and xray absorption spectroscopy (XAS) above. The normalization of the experimental results is arbitrary; they were therefore normalized to the same area as the corresponding parts of the FTPS spectrum in the figure. The absolute position of the XAS spectrum is not well known; for the figure it was shifted by 0.8 eV to lower energies.

The theoretical prediction from FTPS and the experimental result in Fig. 11 then agree rather well, both in the peak structure and in their bandwidths below and above the Fermi energy. Notably, the assignment of orbitals to peaks from the experimental conclusions agrees with those of the theoretical peaks and their atomic nature (similar to table 1 [6]).

Fig. 11: *Spectrum for SrMnO₃ obtained by FTPS compared to experimental results [44], from [6]. The assignment of orbitals to peaks above the Fermi energy is from the experimental paper. Spin up refers to an excitation with majority spin, and spin down with minority spin.*

Encouragingly for the new method, the new FTPS calculations took about the same computational time (about 700 CPU hours on 8 cores) per DMFT iteration as the CTQMC calculations for this full five-orbital calculation, while providing considerably better energy resolution.

5 Conclusions

The new FTPS impurity solver for DMFT is based on the Matrix Product State (MPS) formalism that is also the basis for DMRG, and on tensor extensions thereof. It works by calculating the ground state for an impurity model with a given hybridization function, generating an excitation, and then time evolving it directly in real time. It reaches very good energy resolution even and especially at high energies, impossible to achieve for example with CTQMC. The latter can have an advantage at very small frequencies.

The key new ingredient with respect to numerous earlier MPS based methods is the fork-like structure of Fig. 7, which separates the baths for different impurities and spin directions as much as possible and makes the method very efficient – as fast as CTQMC for three- and five-orbitals in calculations done so far. The FTPS method is very new. Its possibilities and limitations remain to be explored. Further improvements and generalizations are likely possible. The method will hopefully enable new investigations and physical insight in DMFT calculations.

References

[1] W. Metzner and D. Vollhardt, Phys. Rev. Lett. **62**, 324 (1989)

[2] A. Georges, G. Kotliar, W. Krauth, and M.J. Rozenberg, Rev. Mod. Phys. **68**, 13 (1996)

[3] A. Georges, A. Poteryaev, S. Biermann, M. Posternak, A. Yamasaki, and O.K. Andersen,
Phys. Rev. **B 74**, 125120 (2006)

[4] G. Kotliar, S.Y. Savrasov, K. Haule, V.S. Oudovenko, O. Parcollet, and C.A. Marianetti,
Rev. Mod. Phys. **78**, 865 (2006)

[5] D. Bauernfeind, M. Zingl, R. Triebl, M. Aichhorn, and H.G Evertz,
Phys. Rev. **X 7**, 031013 (2017)

[6] D. Bauernfeind, R. Triebl, M. Zingl, M. Aichhorn, and H.G. Evertz,
Phys. Rev. **B 97**, 115156 (2018)

[7] U. Schollwöck, Ann. Phys. **326**, 96 (2011)

[8] S.R. White, Phys. Rev. Lett. **69**, 2863 (1992)

[9] D. Bauernfeind, Ph.D. thesis, Graz 2018

[10] K.G. Wilson, Rev. Mod. Phys. **47**, 773 (1975)

[11] R. Bulla, T.A. Costi, and T. Pruschke, Rev. Mod. Phys. **80**, 395 (2008)

[12] P. Werner, A. Comanac, L. de' Medici, M. Troyer, and A.J. Millis,
Phys. Rev. Lett. **97**, 076405 (2006)

[13] E. Gull, A.J. Millis, A.I. Lichtenstein, A.N. Rubtsov, M. Troyer, and P. Werner,
Rev. Mod. Phys. **83**, 349 (2011)

[14] M. Caffarel and W. Krauth, Phys. Rev. Lett. **72**, 1545 (1994)

[15] M. Capone, L. de' Medici, and A. Georges, Phys. Rev. **B 76**, 245116 (2007)

[16] J. Kolorenc, A.B. Shick, and A.I. Lichtenstein, Phys. Rev. **B 92**, 085125 (2015)

[17] D. Zgid, E. Gull, and G.K.L. Chan, Phys. Rev. **B 86**, 165128 (2012)

[18] Y. Lu, M. Höppner, O. Gunnarsson, and M.W. Haverkort, Phys. Rev. **B 90**, 085102 (2014)

[19] K.M. Stadler, Z.P. Yin, J. von Delft, G. Kotliar, and A. Weichselbaum,
Phys. Rev. Lett. **115**, 136401 (2015)

[20] A. Horvat, R. Zitko, and J. Mravlje, Phys. Rev. **B 94**, 165140 (2016)

[21] K.M. Stadler, A.K. Mitchell, J. von Delft, and A. Weichselbaum,
Phys. Rev. **B 93**, 235101 (2016)

[22] E. Jeckelmann, Phys. Rev. **B 66**, 045114 (2002)

[23] S. Nishimoto and E. Jeckelmann, J. Phys.: Condens. Matter **16**, 613 (2004)

[24] R. Peters, Phys. Rev. **B 84**, 075139 (2011)

[25] M. Karski, C. Raas, and G.S. Uhrig, Phys. Rev. **B 72**, 113110 (2005),
Phys. Rev. **B 77**, 075116 (2008)

[26] T.D. Kühner and S.R. White, Phys. Rev. **B 60**, 335 (1999)

[27] S.R. White and I. Affleck, Phys. Rev. **B 77**, 134437 (2008)

[28] A. Holzner, A. Weichselbaum, I.P. McCulloch, U. Schollwöck, and J. von Delft,
Phys. Rev. B 83, 195115 (2011)

[29] M. Ganahl, P. Thunström, F. Verstraete, K. Held, and H.G. Evertz,
Phys. Rev. **B 90**, 045144 (2014)

[30] F.A. Wolf, I.P. McCulloch, O. Parcollet, and U. Schollwöck,
Phys. Rev. **B 90**, 115124 (2014)

[31] M. Ganahl, M. Aichhorn, H.G. Evertz, P. Thunström, K. Held, and F. Verstraete,
Phys. Rev. **B 92**, 155132 (2015)

[32] F.A. Wolf, A. Go, I.P. McCulloch, A.J. Millis, and U. Schollwöck,
Phys. Rev. **X 5**, 041032 (2015)

[33] ITensor library, http://itensor.org/

[34] G. Vidal, Phys. Rev. Lett. **91**, 147902 (2003)

[35] G. Vidal, Phys. Rev. Lett. **93**, 040502 (2004)

[36] S.R. White and A.E. Feiguin, Phys. Rev. Lett. **93**, 076401 (2004)

[37] A.J. Daley, C. Kollath, U. Schollwöck, and G. Vidal,
J. Stat. Mech.: Theory Exp., P04005 (2004)

[38] E.M. Stoudenmire and S.R. White, New J. Phys. **12**, 055026 (2010)

[39] A. Holzner, A. Weichselbaum, and J. von Delft, Phys. Rev. **B 81**, 125126 (2010)

[40] F.A. Wolf, I.P. McCulloch, and U. Schollwöck, Phys. Rev. **B 90**, 235131 (2014)

[41] P. Schmitteckert, Phys. Rev. **B 70**, 121302 (2004)

[42] D. Bauernfeind and H.G. Evertz, in preparation

[43] T. Barthel, New J. Phys. **15**, 073010 (2013)

[44] D.H. Kim, H.J. Lee, B. Dabrowski, S. Kolesnik, J. Lee, B. Kim, B.I. Min, and J.-S. Kang,
Phys. Rev. **B 81**, 073101 (2010)